An implicit boundary approach for viscous compressible high Reynolds flows using a hybrid remeshed particle hydrodynamics method

Anas Obeidat[a], Stéphane P. A. Bordas[b,a,*]

[a]*University of Luxembourg, Department of Computational Engineering Sciences, Faculty of Science, Engineering and Communication, University of Luxembourg, 6 Avenue de la Fonte, 4364 Esch-sur-Alzette, Luxembourg.*
[b]*Visiting Professor, Institute of Research and Development, Duy Tan University, K7/25 Quang Trung, Danang, Vietnam.*

Abstract

We present an implicit boundary particle method with background mesh adaptation. We use a Brinkman penalisation to represent the boundary of the domain and a remeshed particle method to simulate viscous flow with high Reynolds numbers. A penalty term is added to the Navier-Stokes equations to impose the boundary conditions. The boundary conditions are enforced to a specific precision with no need to modify the numerical method or change the grid, achieving an implicit approach for flow around complex boundaries/geometries simulation. The main idea of the Brinkman penalisation method is to model the solid obstacle as a porous medium. The governing equations for the compressible fluid and penalised Navier-Stokes for the porous medium are solved simultaneously, without need for interface conditions. The accuracy of the method is tested for a number of benchmark problems starting with simple cases such as: a periodic laminar flow in a channel (Poiseuille flow), to more complex problems such as the lid-driven cavity with high Reynolds number, the reflection and propagation of a compressible shock wave, and finally swirling flow in a model two-stroke

---

*Corresponding author
    Email address: `stephane.bordas@uni.lu` (Stéphane P. A. Bordas)

diesel engine. The remeshed particle-mesh method coupled with Brinkman penalisation provides a good quality simulation and the results are in agreement with analytical or reference solutions.

1. Introduction

Many engineering applications require numerical simulations of viscous flows around complex geometries for which the body-fitted grid (BF) method [1], and the immersed boundary (IB) method [2, 3] are the two main approaches.

5   The BF method proposes to generate grids associated with complex boundaries. Consequently, boundary conditions are easily enforced. In order to achieve sufficiently accurate results for flows with high Reynolds numbers, a finer grid for the boundary layer is required. However, generating a good quality fine mesh can be cumbersome, and such meshes lead to substantial computational

10 costs. In moving boundary cases, the simulation setup becomes more complex, expensive as a result of the grid generation process, and the interpolation process of the solution to the new mesh at each computational time step creates projection errors. The BF method can thus be both complex to implement and computationally expensive.

Peskin [4] introduced the IB method as a new approach to study the flow

15

2

around heart valves. Ever since, various immersed boundary techniques have been developed on an alternative approach to the BF method to describe the interaction of fluids with complex geometries. These method had mostly been developed for incompressible viscous flow simulations. Peskin [4] simulated the incompressible flows by solving the NavierStokes equations and the immersed boundary, the momentum equation is modified by employing localised forces to the fluids, and the boundaries are modelled as elastic media, Peskin [4] showed that the boundaries do not need to be massless and that the fluid's density does not need to be uniform.

For rigid obstacle problems Lai [5] extended the method through a stiff spring with restoring force to model an immersed elastic media, this method was later extended by using a feedback force to represent the immersed boundary for solid obstacle problems [6, 7]. However the aforementioned methods have disadvantages, for instance, as they use an explicit time-stepping scheme, requiring small time steps which compromise the efficiency. They are also restricted to non-adaptive grids, making them inefficient for flows with high Reynolds numbers. Lia [5] showed that, in order to mimic the real situation of flow around a solid obstacle, the computational domain must be relatively large compared to the solid obstacle. Moreover, no convergence proof exists for both methods.

Many other IB methods have been developed to simulate incompressible

viscous flow around solid obstacles. In contrast to Peskin's work on immersed boundary method where external forces are employed to simulate the boundaries of the computational domain, Cartesian grid methods [8, 9, 10, 11] and ghost cell immersed boundary methods [12] are IB methods which in contrast to Peskin's method, enforce the boundary conditions directly upon on the immersed boundaries. The Cartesian grid method was extended for compressible flow simulations by Ghias [13], simulating a compressible flow around a circular cylinder and airfoil at high Reynolds number, by modifying the discretised equation near the immersed boundaries. A drawback of this approach is that it does not take in account the acoustic wave reflection and transmission between the solid and fluid at the interface area, which is important for shock wave simulations.

The Brinkman penalisation is another interesting approach to simulate flow around complex geometries, originally proposed by Arquis and Caltagirone [14]. The main idea is to model the complex obstacle as porous media with porosity ϕ and viscous permeability α approach to zero, the boundary conditions are imposed by adding a penalty term to the momentum equations. The Brinkman method has an important advantage: its error bound can be estimated in term of the penalisation parameter [15]. The boundary conditions are enforced to a specific precision with no need to modify the numerical method or adapt the grid. Angot [16] showed that for incompressible Navier-Stokes equations, the method converges to the exact solution as the penalisation parameter approaches zero.

Mittal and Iaccarino [3] pointed that, for high Reynolds number flows the

4

use of IB method techniques will be prohibitively expensive if no adaptive meshes are used in the vicinity of solid walls. Roma et. al. [17] presented an adaptive version of IB method, obtaining a multilevel IB method with self-adaptive capabilities.

Kevlahan and Vasilyev [18] employed the the Brinkman penalisation technique for incompressible flows in the context of adaptive wavelet collocation method.

Another interesting approach is to embed IB method with Isogeometric analysis (IGA) [19, 20] originally introduced by Hughes et. al. [21]. IGA was developed with the purpose to bypasses the mesh generation process required for standard finite element analysis which could potentially reduce the time required for the analysis of complex engineering designs. Schillinger et. al. [19] explored the hierarchical refinement of B-splines of the finite cell method in the framework of immersed boundary analysis, combining B-spline approximations with immersed boundary methods for the simulation of ship propeller and a rim of an automobile wheel. Bazilevs et. al. [22] combined IB with IGA and mesh free descritsation for the simulation of fluid structure interaction.

20

We are aware of other penalty methods like the cut finite element method (CutFEM) approach for extended finite element method (XFEM) [23]. In such methods, the Partial Differential Equations (PDE's) are coupled across the fluid-obstacle interface using a Nitsche-type coupling, while the formulations are pe-

25 nalised by adding ghost-penalty terms in order to enforce the conditions inside the element being cut by the interface.

Mesh free methods such as vortex methods (VM) and Smoothed Particle

Hydrodynamics (SPH) are considered to handle flows past complex geometries. The original work of IB methods by Peskin [4] was developed for the simulation of heart leaflets at physiological Reynolds numbers using VM [4], by coupling the VM with the IBM with the aim to minimise the computational points used to capture the dynamic of the vorticity in complex geometry. The Smoothed Particle Hydrodynamics (SPH) method was introduced independently by Gingold and Monaghan [24], and by Lucy [25], with the aim to simulate astrophysical problems. By discretising the velocity-pressure formulation of the compressible Navier-Stokes equations, by linking the pressure and density of the flow via a state of equation, the SPH methods avoid solving an elliptic problem to determine the velocity.

Over the years SPH has been extended and applied in many areas. Stam and Fiume [26] first used SPH to simulate fire. Müller et al. [27] developed an SPH method which can be applied on real-time fluid simulation. The SPH method was also extended in free surface flows problems [28], and low-Reynolds number viscous flows [29, 30, 31], Cummins et al. [32] extended SPH to simulate incompressible fluids, followed by Shao et al. [33] who propose an SPH simulation for Newtonian and non-Newtonian flows with a free surface. Cleary and Monaghan [34] extended SPH to heat transfer simulation, and finally the method was developed for multi-phase flows simulation by Morris [35].

Turbulence modelling with SPH is a rather new field of research. Mon-

aghan [36] introduced a Lagrangian-averaged Navier-Stokes turbulence model modifying the original SPH method for the simulation of two-dimensional turbulence. Three SPH turbulence models were introduced by Violeau and Issa [37], two algebraic models, and one based on the Reynolds stress model. Dalrymple and Rogers [38] used a large eddy simulation (LES) turbulence model to simulate two-dimensional breaking waves with SPH. Robinson and Monaghan [39] studied how SPH performs in a direct numerical simulation (DNS) of decaying turbulence in a two-dimensional no-slip wall-bounded domain.

In the SPH method, as in all Lagrangian particle methods, particles may

30

7

cluster in one area of the computational domain and spread apart in another as a result of the strain of the flow. When this occurs, the system looses the ability to recover the continuous velocity and density fields, which leads to large inaccuracies of the quantities that are being simulated. A set of solutions are suggested to consistently avoid this problem; [40, 41] extended the SPH method to a regularised SPH (RSPH) in order to improve the accuracy of the method. The main idea of the RSPH method is to redefine the particle distribution at temporal intervals through a mass, momentum, and total energy conserving process. Additionally the smoothing length can vary in space and time by a magnitude based on a problem-specific basis. Remeshed SPH (rSPH) is an alternative approach to overcome particle distortion as proposed by Chaniotis et al. [42, 43], in rSPH the particles are uniformly reinitialised (remeshed) on a regular mesh by interpolating the strengths of the particles to the mesh via interpolation function, then a new set of particles is generated and the moments of the field quantities are interpolated back. This method was later extended by Obeidat and Bordas [44] where a hybrid rSPH is proposed, taking advantage of both the Lagrangian and the Eulerian schemes, as the right hand side of the governing equations is computed on the mesh, and the change of momentum is later interpolated to the particles where the advection takes place.

In the context of particle methods and IBM, Cottet and Maitre [45] com-

bined the immersed interface, and the immersed boundary with VM. Dupuis et. al. [46] combined IBM with lattice boltzmann method, performing a two-dimensional simulation past a cylinder, where they approximated the boundaries on the regular lattice in a staircase fashion and showed that the accuracy of the method depends on the detail of the boundary representation. Finally they used two approaches to exchange the information between the boundary and the grid nodes, the interpolating forcing (IF) and the direct forcing (DF) approach. Morgenthal and Walther [47] presented a two-dimensional immersed interface technique for the Vortex-In-Cell (VIC) method, where the boundary conditions are enforced on the immersed interfaces through momentum terms acting on the mesh. The work of Hieber and Koumoutsakos [48] on particle Immersed Boundary method for simulations using remeshed Smoothed Particle Hydrodynamics (rSPH-IB) is similar to the work Chaniotis et al. [42], as both use particle remeshing to overcome the distortion, whilst maintaining the Particle-Particle interaction. In Hieber and Koumoutsakos, the geometry of the body is described by Lagrangian particle level sets [49] and the solid boundary is described by boundary points associated with an impact zone in the flow domain. The particle-mesh interpolation is necessary for the transfer of the forcing term between the fluid and the obstacle. Hieber and Koumoutsakos split the forcing term into two parts. This approach exhibits small scale oscillations in the pressure profile at complex boundaries, and as a solution a ghost particle set was added.

35   In this work we propose another variant of the immersed boundary methods, in which the boundary conditions are imposed by penalising the governing equations by adding a penalised term. This is often referred to as the Brinkman penalisation.

9

In this paper, we employ Liu's [50] extension of the Brinkman penalisation for compressible flows. We introduce an implicit boundary approach for the simulation of viscous compressible high Reynolds flows around or inside complex geometries. The method is based on the previously proposed hybrid remeshed smoothed particle hydrodynamics method (hrSPH) by Obeidat and Bordas [44]. In the current contribution a mask function is added on the grid to implicitly mark the regions where the solid geometry is located. A penalty term is added to the momentum and the continuity equations. This technique effectively considers the computational domain as a porous medium which may be thought of as a sponge with a porosity and permeability. The penalty term is controlled by the mask function.

In the following sections, we will present the porous media equations, followed by the Navier-Stokes equation for the hrSPH method coupled with the Brinkman penalisation. We will then verify the presented method for several benchmark problems and presenting the high accuracy of the method. The paper is closed with conclusions and recommendations for future work.

2. Porous media equations

In this section we will introduce the porous medium equations for compressible flow in order to obtain the corresponding Navier-Stokes equation for the hrSPH method with Brinkman penalty parameters. The main idea of the Brinkman penalisation method [14] is to model the solid obstacle as a porous medium. The governing equations for compressible fluids and penalised Navier-Stokes for the porous medium are solved simultaneously, since no interface conditions are required. For more details about porous media, the reader is referred to [51, 52, 53].

A porous medium is a material containing pores. The skeletal portion of the material is often called the "matrix", and is interconnected by pores. The pores are typically filled with a fluid (liquid or gas). A porous medium is typically characterised by its porosity ϕ, and permeability α. The flow through permeable media is characterised by two length scales: the size of the pores d, and the macroscopic length L. The porosity ϕ is the fraction of the volume of connected pores over the total volume, allowing the fluid to pass through. The permeability α is a measure of the ability of a material to transmit fluid and is proportional to ϕd^2.

2.2. Continuity equation

The continuity equation for porous media reads:

$$\frac{\partial \rho}{\partial t} = -\frac{1}{\phi} \nabla \cdot (\rho \mathbf{v}), \tag{1}$$

where ρ is the interstitial fluid density, $\frac{\partial}{\partial t}$ is the derivative to the time, and v is the Darcy velocity $\mathbf{v} = (v_1, v_2, v_3)$, $\mathbf{v} = \mathbf{u}\,\phi$. As $\phi \ll 1$, where $\|\mathbf{v}\| < \|\mathbf{u}\|$, $\mathbf{u} = (u_1, u_2, u_3)$ is the interstitial velocity of the fluid.

2.3. Darcy's law, Brinkman equation and extensions

The first Darcy's law reads:

$$\mathbf{v} = -\frac{\alpha}{\mu} \nabla p, \tag{2}$$

where μ is the dynamic viscosity, and p is the intrinsic pressure. In order to meet the no-slip boundary condition, an additional viscous term can be added as follows [54]

$$\nabla p = \frac{\mu}{\alpha} \mathbf{v} + \mu \nabla^2 \mathbf{v}, \tag{3}$$

11

where the first viscous term is the Darcy's term, and the second is the Laplacian term of the Navier-Stokes equation. Wooding [55] extended this expression in order to make it similar to the Navier-Stokes equation, as follows:

$$\rho \left[\phi^{-1} \frac{\partial \mathbf{v}}{\partial t} + (\phi^{-1} \mathbf{v} \nabla)(\phi^{-1} \mathbf{v}) \right] = -\nabla p - \frac{\mu}{\alpha} \mathbf{v}, \tag{4}$$

which was in turn extended to the Brinkman equation by Vafai and Tien [56]:

$$\rho \left[\phi^{-1} \frac{\partial \mathbf{v}}{\partial t} + (\phi^{-1} \mathbf{v} \nabla)(\phi^{-1} \mathbf{v}) \right] = -\nabla p - \frac{\mu}{\alpha} \mathbf{v} + \mu \nabla^2 \mathbf{v}. \tag{5}$$

Finally, Eq. (5) can be rewritten as a volume-averaging method as [56]:

$$\frac{1}{\phi} \frac{\partial \rho v_i}{\partial t} = -\frac{1}{\phi} \frac{\partial}{\partial x_j}(\rho \phi^{-1} v_i v_j) - \frac{\partial p}{\partial x_i} + \mu \frac{\partial^2 v_i}{\partial x_j^2} - \frac{\mu}{\alpha} v_i \tag{6}$$

Beck [57] showed that in Eq. (5) the convection term $(\phi^{-1} \mathbf{v} \nabla)(\phi^{-1} \mathbf{v})$ is inconsistent with the no-slip boundary conditions, and it was subsequently dropped by Nield [51] later.

Since Eq. (5 entails that the momentum decays with the order of $\exp[-(\phi/\alpha)t]$, neglecting the coefficient ϕ^{-1} on the left hand side hardly affects the solution. Consequently, the momentum remains to decay sufficiently fast [50].

Liu and Vasilyev [50] presented a simplified momentum equation with a Brinkman penalisation for compressible flows. Their simplification is possible since the penalisation term results in a significant damping of the momentum inside the porous media whilst the no-slip boundary conditions are satisfied.

2.4. Brinkman penalisation for compressible flow

Starting with the Navier-Stokes equations for compressible flow Eq. (7, 8),

$$\frac{D\rho}{Dt} = -\rho \frac{\partial u_i}{\partial x_i} \tag{7}$$

and the conservation of momentum,

$$\rho \frac{Du_i}{Dt} = -\frac{\partial p}{\partial x_i} + \frac{\partial \tau_{ij}}{\partial x_j} + \frac{\partial \tau_{ij}^{sgs}}{\partial x_j} \tag{8}$$

in which

$$\tau_{ij} = \mu \left(\frac{\partial u_i}{\partial x_j} + \frac{\partial u_j}{\partial x_i} - \frac{2}{3} \delta_{ij} \frac{\partial u_k}{\partial x_k} \right) \tag{9}$$

where $\frac{D\diamond}{Dt} = \frac{\partial \diamond}{\partial t} + (u \cdot \nabla)(\diamond)$ denotes the material derivative, u_i is the velocity, x is the position, p is the pressure, ρ is the density, τ_{ij} is the shear stress, μ is the dynamic viscosity, δ_{ij} is the Kronecker delta, and τ_{sgs} is the sub-grid stress tensor, which is zero for direct numerical simulation. In the presented work we model the turbulent sub-grid stresses using the standard Smagorinsky model [58], defined as

$$\tau_{ij}^{sgs} = \rho \left(C_s \Delta \right)^2 \sqrt{2 S_{ij} S_{ij}} \widehat{S_{ij}} \tag{10}$$

with

$$\Delta = h, \tag{11}$$

where C_s is a non dimensional constant for which values ranging from

0.1 to 0.24 have been suggested in literature [59], Δ is the model length scale which is proportional to the the grid spacing Eq. (11), h are the mesh spacing, $\widehat{S_{ij}} = \frac{1}{2}\left(\frac{\partial u_i}{\partial x_j} + \frac{\partial u_j}{\partial x_i}\right) - \frac{2}{3}\frac{\partial u_k}{\partial x_k}\delta_{ij}$ is the the filtered strain tensor, and $(C_s\Delta)^2\sqrt{2S_{ij}S_{ij}}$ is the norm of the filtered strain tensor, where $S_{ij} = \frac{1}{2}\left(\frac{\partial u_i}{\partial x_j} + \frac{\partial u_j}{\partial x_i}\right)$

In the following, the viscous compressible flow around a set of obstacles O_q is numerically simulated, whilst the velocity on the surface of the obstacle must meet the no-slip boundary condition:

$$\begin{pmatrix} u \\ v \\ w \end{pmatrix} = \begin{pmatrix} u_{oq} \\ v_{oq} \\ w_{oq} \end{pmatrix} \quad \text{on } O_q, \forall q, \tag{12}$$

where (u_{oq}, v_{oq}, w_{oq}) are the three velocity component in the obstacle O_q, and q is the three dimensional obstacle space.

To specify no-slip boundary conditions without directly imposing Eq. (12), we can follow Angot [15] by adding penalty terms to the momentum equation. This extension results in a loss in mass and energy of the waves reflected from the obstacle, producing wrong simulation results. Liu and Vasilyev [50] combined both the Navier-Stokes and porous media equations, resulting in a Brinkman penalisation method for compressible flows:

$$\frac{D\rho}{Dt} = -\left[1 + \left(\frac{1}{\phi} - 1\right)\chi\right]\rho\frac{\partial u_i}{\partial x_i} \tag{13}$$

$$\rho\frac{Du_i}{Dt} = -\frac{\partial p}{\partial x_i} + \frac{\partial \tau_{ij}}{\partial x_j} + \frac{\partial \tau_{ij}^{sgs}}{\partial x_j} - \frac{\chi}{\eta}(u_i - u_{oq}) \tag{14}$$

The system is closed with the equation of state:

$$p = \rho c^2, \tag{15}$$

14

where ϕ is the porosity, $\eta = \alpha\phi$ is the normalised viscous permeability. Note that $0 < \phi \ll 1$, and $0 < \eta \ll 1$. χ is the solid mask, and defined as,

$$\chi_q(x) = \begin{cases} 1 & \text{if } x \in O_q, \\ 0 & \text{Otherwise.} \end{cases} \tag{16}$$

In Eq. (16) the solid mask χ is defined that it is 1 inside the solid and 0 in the fluid.

To improve the numerical accuracy of the rate-of-change of the momentum, χ can be built via a polynomial "quasi-step" function, so that it varies smoothly from 0 to 1. The step function is sketched in Fig. 1.

The step function χ varies smoothly over the smooth interval of width L normal to the surface, coinciding to a fixed number of mesh cells. The step function is a function of the signed distance to the solid surface (normal vector), with 1 inside the solid obstacle and smoothly goes to 0 at the surface of the solid obstacle. The polynomial step function is continuous and differentiable, a second order over the first and last $L/4$ of the interval, and first order in the intermediate region.
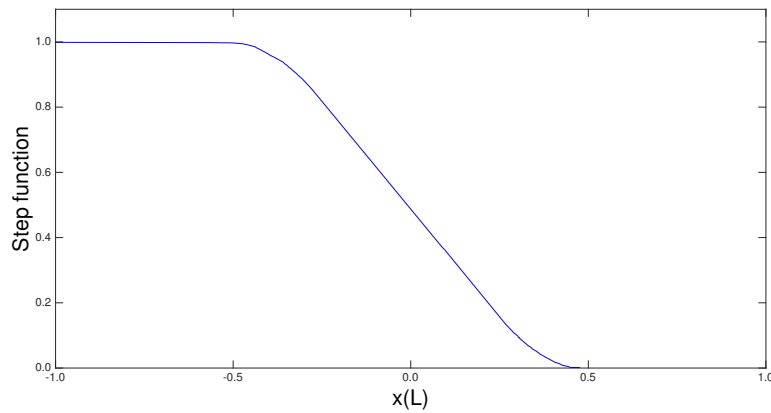
Figure 1: The polynomial step function as a function of the signed distance to the solid surface (second order over the first and last $L/4$, and first order in the intermediate region).

15

3. Brinkman penalisation with hrSPH method

After defining the computational domain and initialising the mesh field on the mesh, the solid geometry is read as stereolithography triangulation (STL) file format containing a triangulated surface representation of an object through triangles described by three corner points and a normal, this file is called an STL patch. Then the χ fields on the nodes are initialised as a smooth step function by intersecting the computational mesh with the triangulated surface; the desired obstacle velocity U_0 is initialised. Subsequently, the hrSPH method is used directly without altering the numerical scheme; it intrinsically deals with the term $\frac{\chi}{\eta}(u - u_o)$ (the penalisation field). For more details regarding the hrSPH method and the algorithm, the reader is referred to [44], a short summery of the hrSPH method is illustrated next.

Our method is divided into three parts:

1. Computing the rate of change

   (a) Particle-mesh interpolation of the mass and impulse of the particle.

$$m(x_m) \quad = \quad \sum_{x_p \in \mathbb{P}(m)} m_p \ W(x_m - x_p, h), \qquad (17)$$

$$m(x_m)u(x_m) \quad = \quad \sum_{x_p \in \mathbb{P}(m)} m_p u_p \ W(x_m - x_p, h), \qquad (18)$$

where $\mathbb{P}(m)$ denotes the set of particles that contribute to mesh node x_m, h the particle spacing, W the high order kernel, u_p the three velocity component u, v, w, m_p the mass of the particle, x_m the position of mesh node m, and x_p the position of particle p.

16

(b) On the grid, obtain the velocity from the interpolated impulse

$$u(x_m) = \frac{m(x_m)u(x_m)}{m(x_m)} \tag{19}$$

(c) On the grid, compute the fluid density from the interpolated mass and the pressure from the equation of state Eq. (15).

$$\rho(x_m) = \frac{m(x_m)}{h^3} \tag{20}$$

(d) On the grid, compute the rate-of-change of the fluid momentum on the mesh (Δu_m) using finite-differences.

(e) The rate-of-change of momentum is interpolated from the grid to the particles (Δu_p).

$$\Delta u(x_p) = \sum_{p=1}^{N} \Delta u_m, W(x_m - x_p, h) \tag{21}$$

2. Updating the particles

This part takes place on the set of particles, where the interpolated rate of change in velocity is used to update the velocity and position of the particles.

$$\vec{u}_p^{t+1} = \vec{u}_p^t + \Delta \vec{u}_p \Delta t \tag{22}$$

$$\vec{x}_p^{t+1} = \vec{x}_p^t + \vec{u}_p^{t+1} \Delta t \tag{23}$$

3. Remeshing the particles:

In case of distortion and particle clustering (high CFL number, high gradients), interpolate the strengths of the particles to the mesh via $M'4$ interpolation function, generate a new set of the particles, interpolate the

17

strengths back to the new set of particles.

The $M'4$ introduced by [60], interpolates the strength of the particles to the mesh, the strengths are redistributed onto the surrounding mesh nodes. The redistribution of particle quantities is achieved using the 3rd order $M'4$ kernel which in one dimension is expressed as:

$$M'4(x,h) = \begin{cases} 1 - \frac{5s^2}{2} + \frac{3s^3}{2} & 0 \le s < 1, \quad s = \frac{|x|}{h} \\ \\ \frac{(1-s)(2-s)^2}{2} & 1 \le s < 2, \\ \\ 0 & s \ge 2, \end{cases} \tag{24}$$

where $|x|$ is the distance of the particle to the mesh, h is the spacing of the new uniform set of particles.

4. Verification for Brinkman penalisation with hrSPH method

To validate the hrSPH method with Brinkman penalisation, we test a series of benchmark problems:

- Flow through a channel (Poiseuille flow); to verify the implicit boundary approach using the hrSPH method solution with the classical analytical Poiseuille flow solution.

- Lid-driven cavity; here we simulate the moving top wall with a constant velocity $U_{max} = 1$ as $U_o = 1$, and we simulate the viscous flow with high Reynolds number to validate the method.

- Compressible shock wave; a real compressible flow with high Mach number.

18

- Swirling flow in a modelled two-stroke diesel engine; where we study the axial and tangential velocity profile in a simplified two-stroke engine.

4.1. Poiseuille flow

The Poiseuille flow is a classical test case for laminar flow in a pipe for which the analytical solution is known.

We study the flow through a 2D channel. The computational domain is a periodic rectangle with length L and width $L/2$. At the centre of the domain, a solid wall is represented as a penalised region, where the STL patch (triangulated surface) with length L and width $L/5$ is located as shown in Fig. 2.

Simulating the flow through a channel with a solid wall in the centre of the computational domain is the simplest way and requires no additional work to impose symmetry. The upper part represents the upper half of the channel, whereas the lower part is the other half. The simulation is started with a uniform density ρ and zero velocity $U = (u, v, w)$, external force in x-direction, with $\phi = 1 \times 10^{-2}$, and $\alpha = 2 \times 10^{-2}$.

Several computational domain resolutions were tested to study the spatial convolution. We start with 32×32 particle and stop with 256×256 particles, resulting in mesh spacings of $\Delta x/L = 0.28$, 0.14, 0.07, 0.035. Note that the resolution of the triangulated surface (STL patch) can remain the same, even though the resolution of the computational mesh varies.

(a)   (b)
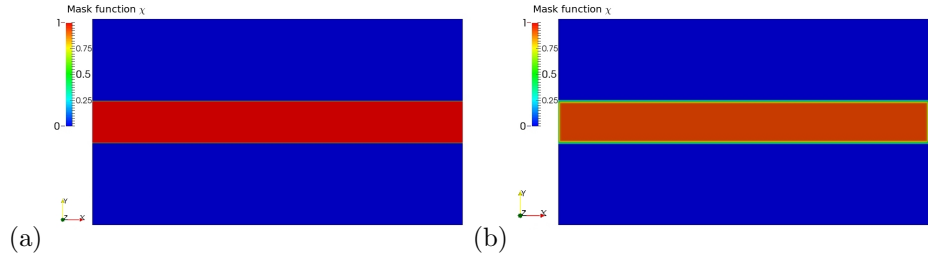
Figure 2: The computational domain for the 2D Poiseuille flow with the penalised area as a Heaviside mask function (a) (χ), and (b) as a smooth step mask function (χ).

Fig. 3 represents the simulated flow as velocity vector, which helps more to understand the computational domain.
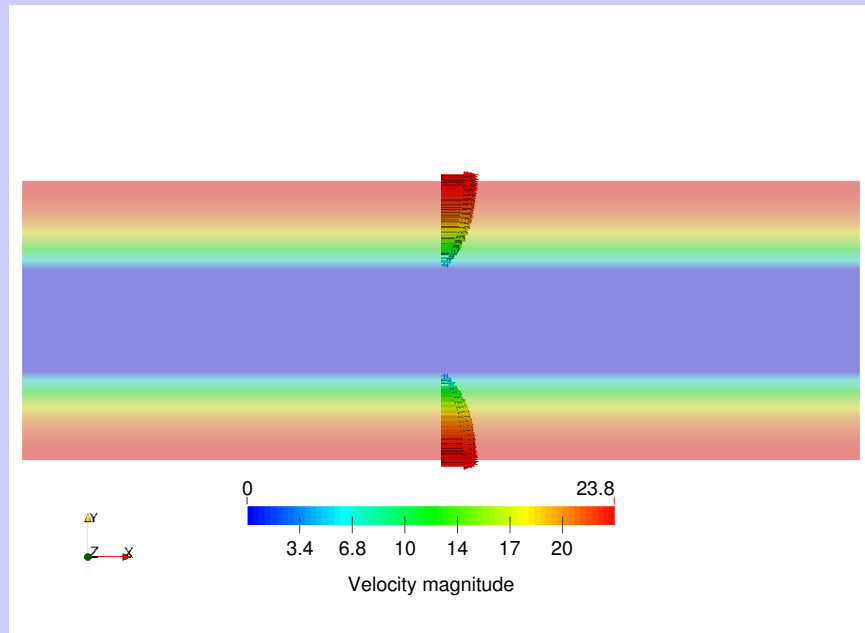

Figure 3: Velocity vector fields of the Poiseuille flow for the hrSPH method with Brinkman penalisation, where the boundary layer are represented.

The simulated Poiseuille flow using the hrSPH method with Brinkman penalisation at different resolutions is shown in Fig. 4 for different resolutions of the computational grid, where u/U_{max} is extracted over the y-axis from the top of the channel till the centre of the penalised area.

Fig. 4 represents the normalised velocity profiles for different resolutions of the computational grid, where u/U_{max} is extracted over the y-axis from the top of the channel to the centre of the penalised area. The Brinkman penalisation is able to reduce the velocity to zero. The results become more accurate with an increase in the resolution of the mesh.

20
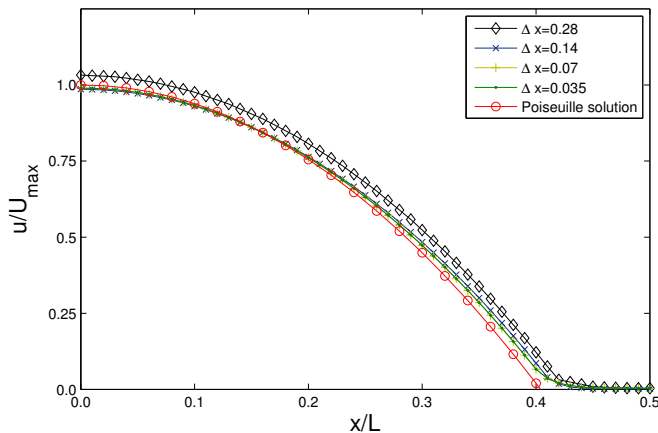
Figure 4: The normalised velocity magnitude of the Poiseuille flow with a different resolution along with the analytical solution for the hrSPH method with Brinkman penalisation. The surface of the penalised area successfully managed to represent the required no-slip boundary condition at the channel surface at $x/L \approx 0.4$, forcing the normalised velocity u/U_{max} to drop to ≈ 0 as a result of the penalty term.

Fig. 4 illustrates how the surface of the penalised area successfully managed to represent the required no-slip boundary condition at the channel surface at $x/L \approx 0.4$, forcing the normalised velocity u/U_{max} to drop to ≈ 0 as a result of the penalty term. Note that only two cells are required to represent the smooth stepping on the solid surface. The pace convergence study is represented in Fig. 4, where we simulated the flow with 4 different mesh resolutions, as shown in Fig. 4 the finer the resolution the closer the solution to converge to the exact solution, up to a level of refinement, where refining the mesh more does not affect the solution.

In Fig. 5 we show the effect of applying a smooth step function on the penalised mask χ compared to applying a Heaviside function, for accurate representation of the no-slip boundary condition.

The velocity profile when the smooth mask function is used, is stepping smoothly toward the wall (channel wall) and needs around 2 cells inside the penalised area acting as boundary layer to represent the no-slip boundary con-

21

dition. On the other hand the Heaviside function represents the no-slip condition approximately at the channel wall.
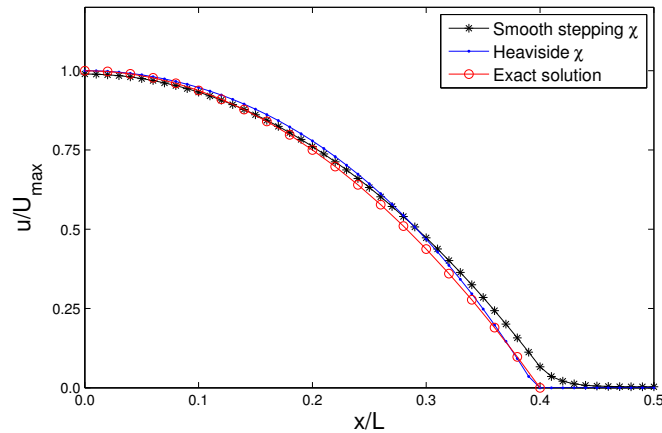

Figure 5: The normalised velocity magnitude of the Poiseuille flow simulated using a Heaviside mask function (χ), and a smooth step mask function (χ) to represent the penalised term, together with the analytical solution.

4.2. Lid-driven cavity

In the second benchmark problem, we consider the lid-driven cavity problem using the hrSPH method with Brinkman penalisation. When simulating the lid-cavity, two difficulties arise. First, singularities at the top corners appear due to the lid moving horizontally and the no-slip conditions on the vertical walls. The second difficulty is the high velocity gradients that arise at high Reynolds numbers.

The computational domain is a unit square with length L and the top wall is moving with a constant speed $U_{\max} = 1$. The computational domain is completely bounded by an STL patch to represent the domain walls using the Brinkman penalisation method Fig. 6. To simulate the moving top wall, an extra STL patch is introduced , which is given a constant speed $U_{\max} = 1$ as $U_s = 1$ which will represent the moving wall, as seen in Fig. 6.

22
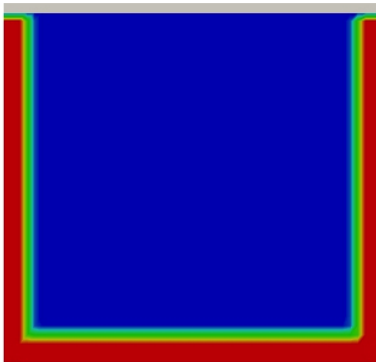
Figure 6: The Lid-driven cavity computational domain, with the bounded penalised walls represented as a step function. The moving top wall is presented in grey.

Three different Reynolds number $Re = (10^2, 10^3,$ and $10^4)$ are simulated with Mach number $Ma = 0.1$.

As no analytical solution for the Lid-driven cavity problem exists, we use the results of Ghia [61] as a reference solution. Ghia used a highly-resolved multi-grid finite difference method with 257×257 grid. For the hrSPH method with Brinkman penalisation two grid resolutions are tested to capture the structure of the flow, 100×100 and 200×200 particles, yielding $\Delta x = 0.01, \Delta x = 0.005$. The results after a steady state occurs, are extracted and compared with the reference solution. The steady state is reached when the total kinetic energy remains constant in time.

Fig. 7(a) presents the steady state field for $Re = 10^2$ with $\Delta x = 0.01$. The velocity magnitude ranges from zero (blue) to $U_{\max} = 1$ red, along with the velocity vector fields, which represent the structure of the flow. As a result of the shear force on the moving wall, a single vortex core occurs in the top half

of the domain. At the bottom the fluid is moving relatively slowly.

To compare the computed flows with those of Ghia we extract the velocity in the y-direction across a centreline in the x-direction $(U_y(x))$, and the velocity in the x-direction across a centreline in the y-direction $(U_x(y))$. Fig. 8(a) illustrates the computed profiles for $Re = 10^2$ over the horizontal, and vertical centrelines. Both velocity profiles show a good agreement with Ghia's reference solutions [61].

The velocity fields for the higher Reynolds number at $Re = 10^3$ and 10^4 are presented in Fig. 7(b), and Fig. 7(c). For an increase of the Reynolds number, the vortex core moves clearly to the centre of the domain, and the intensity of the vortex increases as well. The velocity also increases in the bottom part of the cavity. The coarse grid with $(\Delta x = 0.01)$ failed to accurately predict the vortex location for both higher Reynolds number $Re = 10^3$ and 10^4, as can be seen in Fig. 8(b), and Fig. 8(c), where both velocity profiles $(U_x(y))$, $(U_y(x))$ are slightly shifted off the reference solution. To capture the flow structure at $Re = 10^3$, a finer grid with $\Delta x = 0.005$ is used. Employing this grid, the solution shows a good agreement with Ghia's results as the velocity profiles illustrate.

For the error analysis of the hrSPH simulation, the relative error (L_∞) is used

$$L_\infty(t) = \left| \frac{\min(U_{x(y),hrSPH}) - \min(U_{x(y),exact})}{\min(U_{x(y),exact})} \right|, \tag{25}$$

where, $U_{x(y),hrSPH}$ is the numerical velocity component U_x across in the

24

y-direction, and $U_{x(y),exact}$ is the exact one from [61].

In Fig. 9 the hrSPH simulation with 100×100 particle sustain an error $(L_\infty < 5\%)$ and grid independent for $Re = 10^1$ to 10^3, however it is essential to increase the resolution for Re higher than 10^3 Fig. 9.

Finally we tested the convergence rate of the relative error L_∞ for a spatial grid refinement. The profile of the relative error (L_∞) of the hrSPH simulation with different number of particles per dimension $[64, 100, 128, 200, 256, 300, 512]$ at $Re = 10^3$ is presented in Fig. 10, Fig. 10 illustrate that the L_∞ decreases as the number of particles increases.

225

(a) $Re = 10^2$

(b) $Re = 10^3$

(c) $Re = 10^4$

Velocity magnitude
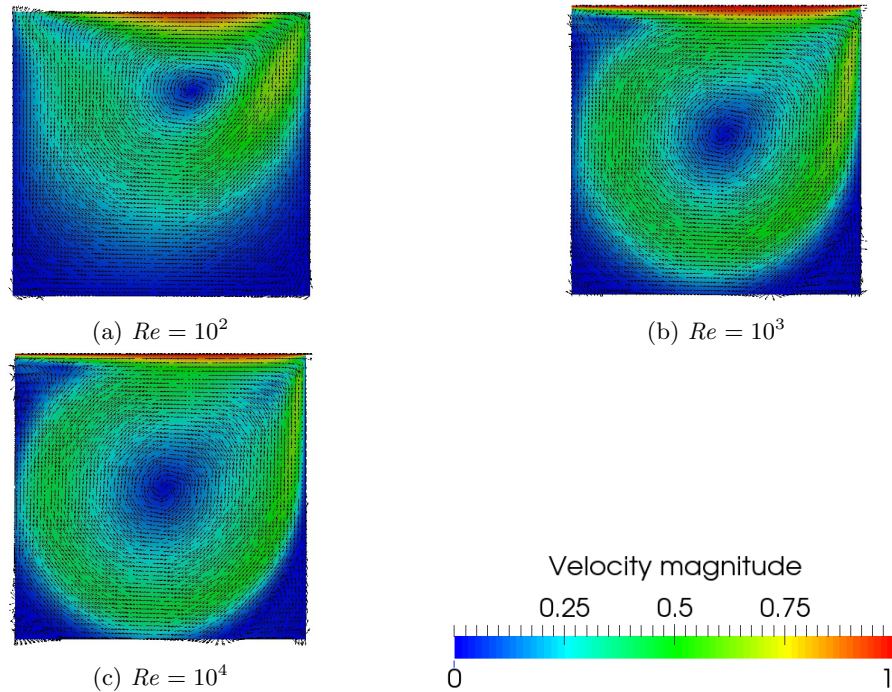
Figure 7: The velocity fields (magnitude and direction) computed for the lid-driven cavity problem for different Reynolds numbers.

25
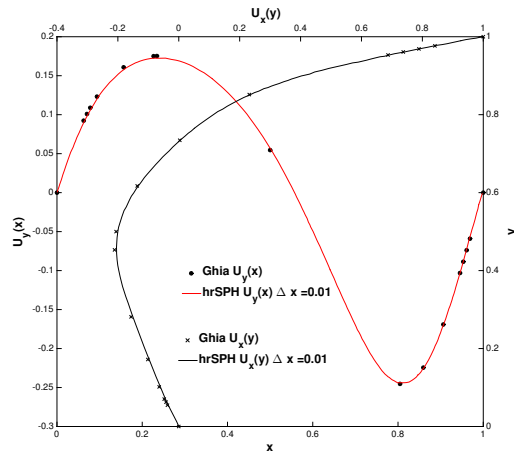
(a) $Re = 10^2$
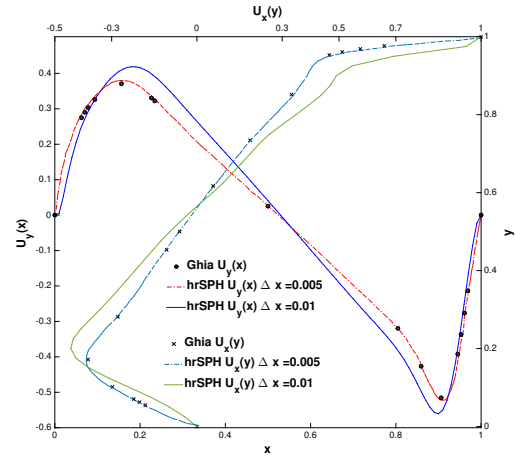
(b) $Re = 10^3$
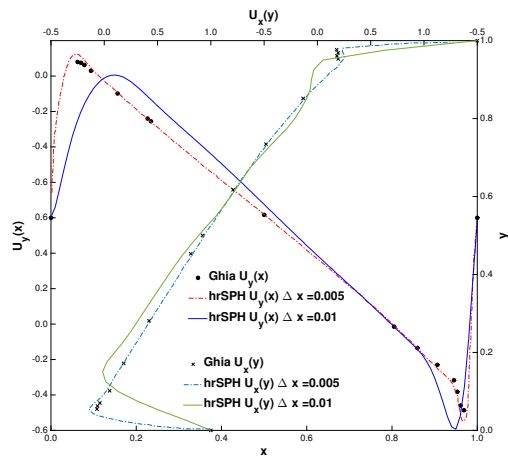
(c) $Re = 10^4$

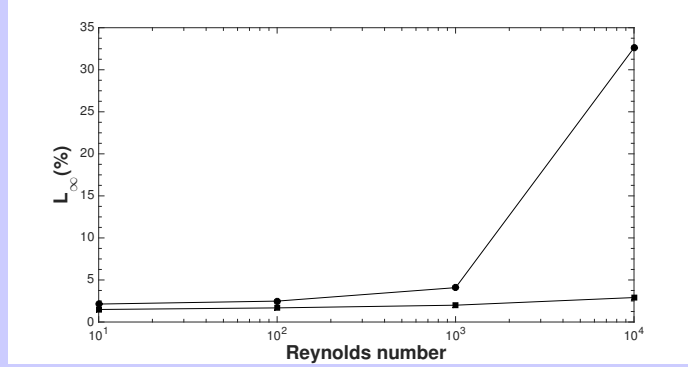Figure 8: The velocity profiles for the lid-driven cavity problem compared to those of Ghia [61].

Figure 9: (L_∞) error of the hrSPH simulations of the lid-driven cavity flow for different Reynolds number with two different grid resolution (100×100) (●) and (200×200) (■). The maximum of the relative error (L_∞) is less than 5% for Re in the range considered $10^1 - 10^3$, where the hrSPH is grid independent, but for larger Re the number of particles needs to be increased.
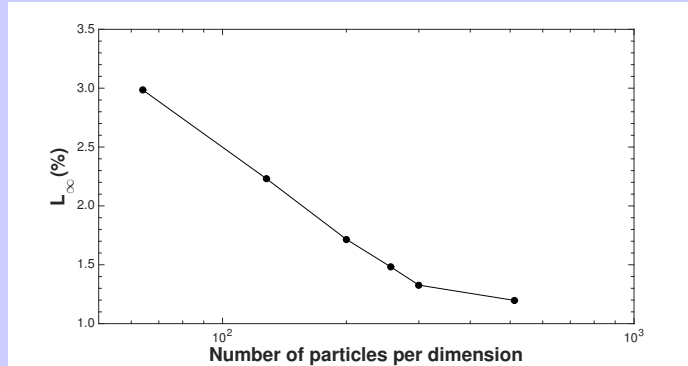
Figure 10: (L_∞) error of the hrSPH simulations of the lid-driven cavity flow with different resolutions and $Re = 10^3$.

4.3. Compressible shock wave

To simulate a compressible flow exposed to a shock wave, a rectangular computational domain $[-L, 2L], [-L, L]$ with periodic boundary conditions, a penalised cylinder with radius $L/10$ at the centre of the computational domain is considered (see Fig. 12(a)). The initial conditions are pressure perturbations

p' resulting from a Gaussian distribution [50]:

$$p' = 10^{-3} \exp\left[-\ln(2)\left(\frac{(x-4)^2 + y^2}{0.04}\right)\right] \qquad (26)$$

with the following initial density:

$$\rho = 1 + p'. \qquad (27)$$

In this case $\phi = 0.02$, and $\alpha = 0.05$ are used.

The initial pressure perturbations form an acoustic wave which propagates towards the solid cylinder at the origin of the computational domain, as illustrated in Fig. 11(a). When the wave front reaches the solid cylinder, it reflects, thereby producing a second wave propagating in the opposite direction. The main wave splits into two parts as a result of the interaction with the solid cylinder and continues to move in the same direction as shown in Fig. 11(b), which represents an instantaneous snapshot of the pressure perturbation in time $t = 4.0$. In time $t = 6.0$ the two parts of the main wave collide and merge on the left side of the solid cylinder producing a third wave, as shown in Fig. 11(c). In Fig. 11(d) the reflected wave and the main one both continue to propagate towards the boundaries and completely surround the solid cylinder.

The main issue in this example is the method's ability to capture the physical structure of the reflected wave and the third propagated wave. The quality of the reflected wave and the third propagated one strongly depends on how well the Brinkman penalisation method can map the solid cylinder in the computational domain and how well the no-slip condition is incorporated. Five points around the cylinder are marked as sample points (A-E in Fig. 12(a)), and the time history of the perturbation pressure is extracted. As the flow is symmetric around the x-axis, only the upper side of the cylinder is covered with the sample

28

points, points A and E are important to observe the quality of the reflected wave and the third propagated wave.

The numerical results are shown in Fig. 12(b-e), together with the exact solution (which is taken from [50]). Fig. 12(b) shows the perturbation pressure of the main wave at time $t \approx 2.0$ and, later the reflected wave at time $t = 4.0$ and later at time $t = 5.0$ for point B. Fig. 12(e) presents the perturbation pressure of the third wave after the two separated waves merge and collide. All the numerical results show a good agreement with the exact solution, indicating the ability of the hrSPH method coupled with the Brinkman penalisation to capture the correct physics of the propagating waves, which is a result of the method's correct representation of the no-slip boundary condition.

(a) time = 2

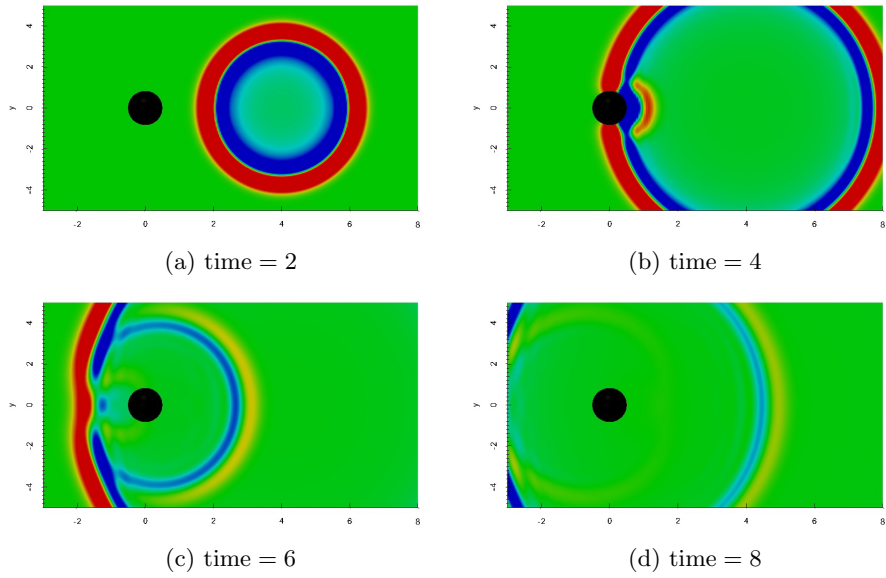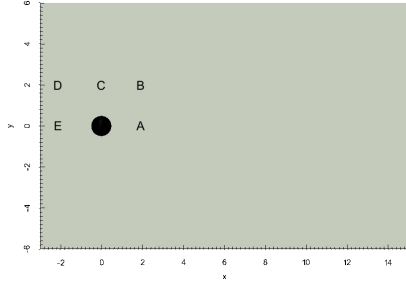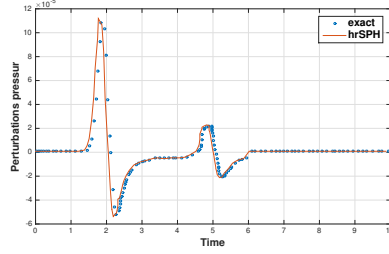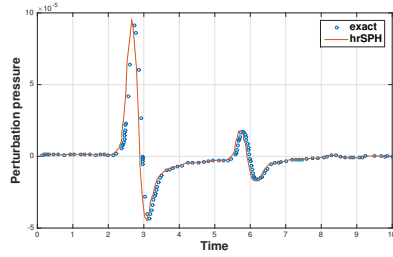(b) time = 4

(c) time = 6

(d) time = 8
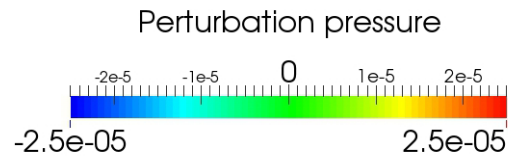
Figure 11: Pressure perturbation profiles computed for the compressible flow exposed to a shock wave at $t = 1.0$, $t = 4.0$, $t = 6.0$ and $t = 8.0$
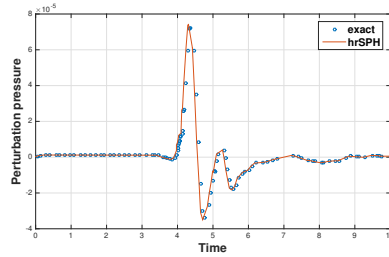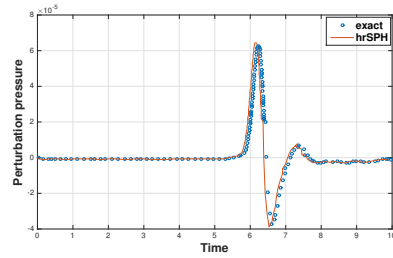
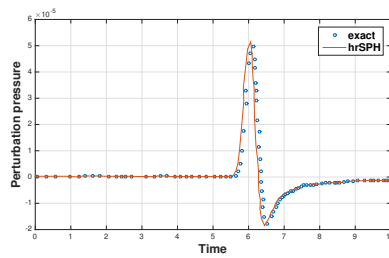(a) The five sampling points in the domain.

(b) Sampling point A.

(c) Sampling point B.

(d) Sampling point C.

(e) Sampling point D.

(f) Sampling point E.

Figure 12: Compressible shock wave perturbation pressure responses for the compressible flow exposed to a shock wave at five points.

4.4. Swirling Flow in a Model of Two-Stroke Diesel Engine

To validate the ability of the presented method to simulate flow in a complex geometry, we simulate the in-cylinder swirling flow in a simplified model of a large two-stroke marine diesel engine. Considering the complexity of the real engine, we designed the engine model in a simplest possible way. The setup contains no moving parts, the combustion is neglected and the exhaust valve is discarded. This setup nevertheless allows us to study fundamental aspects of

31

a swirling flow in a uniform scavenged engine. The results are compared with those of another study by Obeidat [62].

4.4.1. The computational domain

The computational domain and the boundary conditions follow the one described in Obeidat et. al. [62]. The computational domain is sketched in Fig.13; it consists of an inlet section, a cylinder, an exhaust pipe and an outlet. The cylinder radius is R and all other dimensions are shown in Fig.13. the flow enters uniformly along a direction perpendicular to the cylinder axis, with an azimuthal velocity component which ensures the overall in-cylinder swirling flow.

We followed Obeidat et. al. [62] boundary condition formula. To be consistent with the $26°$ flow angle measured in [63], a uniform radial and tangential velocity at the inlet is defined with a constant radial speed $V_{r,i} = 0.23V_b$ and a constant tangential speed $V_{\theta,i} = 0.11V_b$. At the outlet we require a zero velocity gradient. We simulate the flow using the hrSPH method on a grid with approximately 4 million cells, whereas 8 million cells were used in Obeidat [62] to achieve satisfactory results compared to the experimental ones. The time step is chosen such that the solution is stable and the Courant number remains below 1 ($u\Delta t/\Delta x < 1$). This is satisfied with a time step $\Delta t V_b/L_c = 3.4 \cdot 10^{-4}$, where V_b is the bulk average flow speed in the cylinder and L_c is the length of the cylinder. We study only the case in which the piston is completely open.
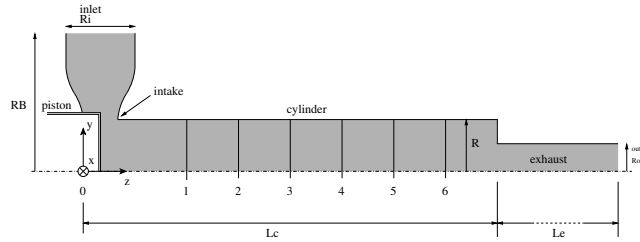

Figure 13: Sketch of the cylindrical computational domain in grey. The flow enters the domain through the horizontal inlet section and exits the domain through the vertical outlet. Notice that the exhaust is shortened in the figure. Data are extracted at the cross-sectional planes $z_{0-6}/R = (0.00, 1.72, 2.77, 3.82, 4.87, 5.93, 6.98)$.

Figure 14: The cylindrical computational domain for the simplified model of a large two-stroke marine diesel engine, including the bounded penalised walls as a mask step function.

285   *4.4.2. results*

The mean axial and tangential velocity profiles are extracted at three cross-sectional planes $z_1/R = 1.72, z_3/R = 3.82$ and $z_5/R = 5.93$ and compared to the results obtained by Obeidat et. al. [62].

The flow is characterised by Reynolds number $Re = \frac{2RV_b\rho}{\mu} = 3 \cdot 10^4$, the

290   simulation is run such that a non-dimensional time $T = tV_b/L_c = 30$.

We consider the case of fully open intake conducted by Obeidat et. al. [62] . We compare the mean velocity profiles and comment on the three-dimensional mean velocity field results simulated by the hrSPH method along with the experimental measurement .In Fig. 15 the mean axial and tangential velocity profiles are shown for three streamwise positions z_1, z_3, z_5, cf. Fig. 13. The measured mean axial profiles are symmetric with a velocity deficit in the central region, resulting in a wake-like profile. The measurements show plateaus with a high axial velocity ($V_z/V_b \approx 2.0$), and a central velocity deficit with the axial velocity reduced to $V_z/V_b = 0.16$, cf. Fig. 15a. It is seen that the hrSPH managed to capture the expected wake-like profile,however the hrSPH under-predicts the velocity deficit, but it over-predicts the plateaus with high axial velocity. Nevertheless, in the downstream cross section Fig. 15c,e the hrSPH recovered and managed to capture the expected velocity deficit at $x/R = 0.0s$.

In the downstream cross sectional plane shown in Fig. 15c, the axial velocity profile retains its wake-like profile although it is widened by diffusion and at z_5 (Fig. 15e) the axial profile is reduced to a plug flow. Note from Fig. 15c,e that at these positions the numerical model resolves qualitatively the wake-like axial

295   profile, although they over-predict in the velocity magnitude at $x/R \lessapprox 0.4$.

The measured and simulated tangential velocity profiles agree well Fig. 15 (b,

33

d, f). It is interesting to note that the hrSPH method show a minor shift in the location of V_θ at positions z_1 Fig. 15 (*b*), and slightly over predicted the velocity magnitude at z_3, z_5 Fig. 15 (*d, f*) compared to the measurement. However, we should note here that for the hrSPH model the grid resolution is around 4 million compared to the 8 million used by Obeidat et. al. [62], additionally, we are using the simplest turbulence model (Smagorinsky). When enough resources are put down to develop a Large eddy simulation model, we expect that the hrSPH method will be able to give a more accurate results for such a high Reynolds number and comparatively coarser mesh. Finally Fig. 16 illiustrates the time-averaged velocity magnitude, notice that the measured and simulated wake-like profile is clearly represented in Fig. 16 (*a*), the recirculation zone is located downstream of the corner where the flow turns from a predominantly radial to a predominantly axial direction. We estimate the streamwise extend of the separation zone from the sign of the axial velocity close to the cylinder wall.
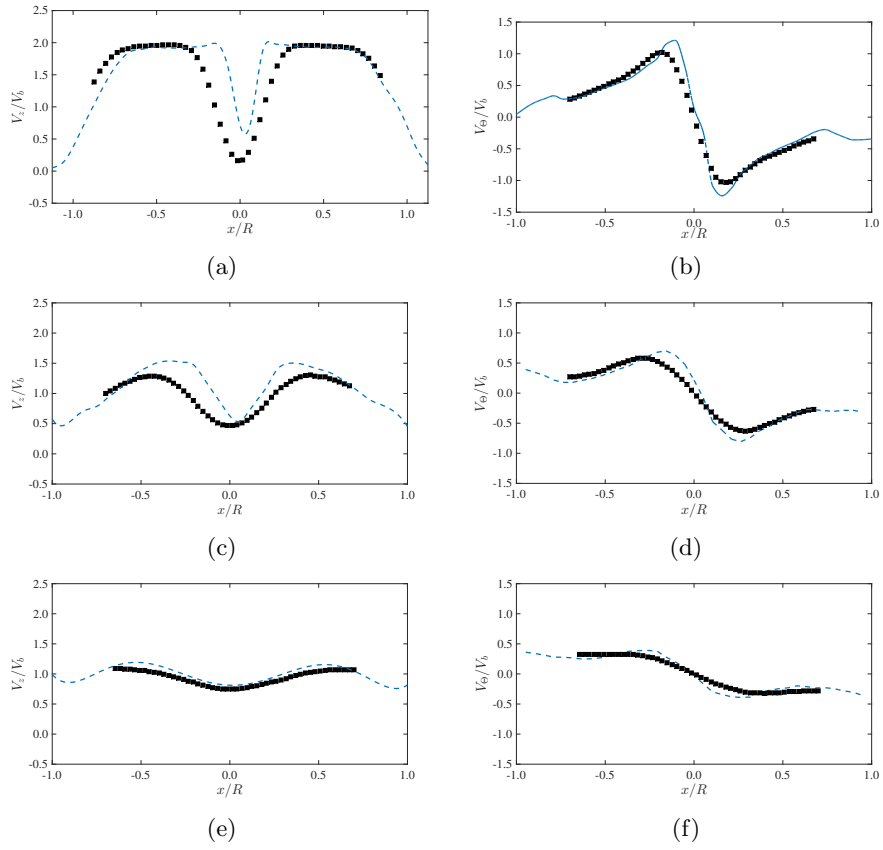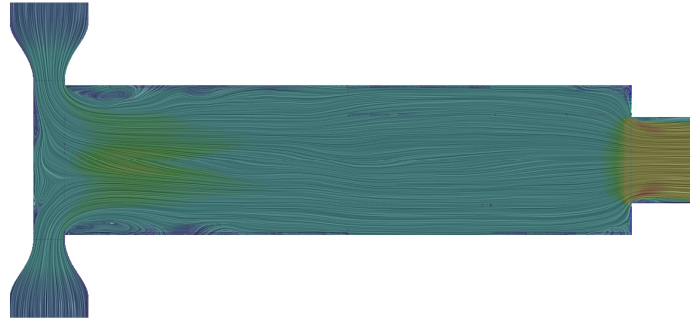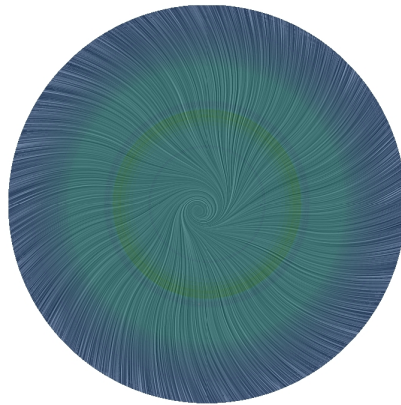
34

Figure 15: The time averaged velocity profiles for the 100% open port case. The axial (a,c,e) and tangential (b,d,f) profiles are obtained at the axial positions (a,b) z_1; (c,d) z_3; (e,f) z_5. Using the hrSPH with smagorinsky model ($--$), and the experimental measurements (■).

(a)

(b)

Figure 16: (a) the meridional planes showing the mean velocity magnitude and the selected stream lines show recirculation zones. (b) The front inlet plane showing the mean velocity magnitude, together with the stream lines exposing the swirl of the flow at the intake toward the cylinder.

5. Summary

The Brinkman penalisation technique coupled with the hybrid-remeshed smoothed particle hydrodynamics, presented in this paper, is a simple approach to simulate flow around solid geometries.

36

The technique is efficient to implement as there is no need to modify the hrSPH numerical scheme, only a penalty term is added to the governing equations, by imposing a mask function on the mesh. The mask function adopts a unit value wherever a solid obstacle is present in the computational domain, zero otherwise.

A number of benchmark problems are presented to test the accuracy of the method, including realistic applications, such as the in-cylinder swirling flow in a simplified model of a large two-stroke marine diesel engine. The results were found in good agreement with reference solutions. We are willing to extend the potential of this method to multiphase flow, where we are working on an implicit interface for multiphase flow problems, applying the mask function on the different flows. Moreover, in the field of Data Science, data-driven modelling is a rising discipline, precisely when a limited amount of measurement data is available in the applications. The method can be applied to a field inversion on the effects of the complex structures of the flow.

References

[1] J. Thompson, Z. U. A. Warsi, C. W. Mastin, Boundary fitted coordinate systems for numerical solution of partial differential equations a review,, J. Comput. Phys. 47 (1982) 1–108.

[2] C. S. Peskin, The immersed boundary method, Acta Numerica (2002) 479–517.

[3] R. Mittal, G. Iaccarino, Immersed boundary methods, Annu. Rev. Fluid Mech. 37 (2005) 239–261.

[4] C. Peskin, Flow patterns around heart valves: A numerical study, J. Comput. Phys. 10 (1972) 252–271.

[5] M.-C. Lai, C. S. Peskin, An immersed boundary method for formal second-order accuracy and reduced numerical viscosity, J. Comput. Phys. 160 (2000) 705–719.

[6] D. Goldstein, R. Handler, L. Sirovich, Modeling a no-slip flow boundary with an external force field, J. Comput. Phys. 105 (1993) 354–366.

[7] E. Saiki, S. Biringen, Numerical simulation of a cylinder in uniform flow: Application of a virtual boundary method, J. Comput. Phys. 123 (1996) 450–465.

[8] J. W. Purvis, J. E. Burkhalter, Prediction of critical mach number for store configurations, AIAA J. 11 (1979) 1170–1177.

[9] D. K. Clarke, M. D. S. H. A., Hassen, Euler calculations for multielement airfoils using cartesian grids, AIAA J. 24 (3) (1986) 353–358.

[10] D. D. Zeeuw, K. G. Powell, An adaptively refined cartesian mesh solver for the Euler equations, J. Comput. Phys. 104 (1993) 56–68.

[11] H. P. Bui, S. Tomar, S. P. Bordas, Corotational cut finite element method for real-time surgical simulation: application to needle insertion simulation, arXiv:1712.03052 (2017) –.

[12] Y. H. Tseng, J. H. Ferziger, A ghost cell immersed boundary method for flow in complex geometry, J. Comput. Phys. 192 (2003) 593–623.

[13] R. Ghias, R. Mittal, T. S. Lund, A non-body conformal grid method for simulation of compressible flows with complex immersed boundaries, AIAA J. (2004) –.

[14] E. Arquis, J.-P. Caltagirone, On the hydrodynamical boundary-conditions along a fluid layer porous-medium interface - application to the case of free-convection, C. R. Acad. Sci. II 229 (1) (1984) 1–4.

[15] P. Angot, C. H. Bruneau, P. Fabrie, A penalization method to take into account obstacles in incompressible viscous flows, Numer. Math. 81 (1999) 497–520.

[16] P. Angot, Analysis of singular perturbations on the Brinkman problem for fictitious domain models of viscous flows, Math. Meth. Appl. Sci. 22 (1999) 1395–1412.

[17] A. M. Roma, C. S. Peskin, M. J. Berger, An Adaptive Version of the Immersed Boundary Method, J. Comput. Phys. 153 (2) (1999) 509–534.

[18] N. K.-R. Kevlahan, O. V. Vasilyev, An adaptive wavelet collocaton method for fluid-structure interaction at high Reynolds numbers, SIAM J. Sci. Comput. 26 (6) (2005) 1894–1915.

[19] D. Schillinger, L. Dedé, M. A. Scott, J. A. Evans, M. J. Borden, E. Rank, T. J. R. Hughes, An isogeometric design-through-analysis methodology based on adaptive hierarchical refinement of nurbs, immersed boundary methods, and t-spline cad surfaces, Comp. Meth. Appl. Mech. & Engng. 249–252 (2012) 116–150.

[20] D. Kamensky, M.-C. Hsu, D. Schillinger, J. A. Evans, A. Aggarwal, Y. Bazilevs, M. S. Sacks, T. J. R. Hughes, An immersogeometric variational framework for fluidstructure interaction: Application to bioprosthetic heart valves, Comp. Meth. Appl. Mech. & Engng. 284 (2015) 1005 –.

[21] T. J. R. Hughes, J. A. Cottrell, Y. Bazilevs, Isogeometric analysis: CAD, finite elements, nurbs, exact geometry and mesh refinement, Comp. Meth. Appl. Mech. & Engng. 194 (39) (2005) 4135–4195.

[22] Y. Bazilevs, G. Moutsanidis, J. Bueno, K. Kamran, D. Kamensky, M. C. Hillman, H. Gomez, J. S. Chen, A new formulation for air-blast fluid–

390   structure interaction using an immersed approach: part ii—coupling of iga and meshfree discretizations, Chem. Mater. 60 (1) (2017) –.

[23] E. Burman, S. Claus, P. Hansbo, M. Larson, G. Mats, A. Massing, Cutfem: Discretizing geometry and partial differential equations, Int. J. for Numer. Methods In Engng. 104 (7) (2015) 472–501.

[24] R. A. Gingold, J. J. Monaghan, Smoothed particle hydrodynamics: theory and application to non-spherical stars, MONTH Notices Roy. Astron. Soc. 181 (1977) 375–389.

[25] L. B. Lucy, A numerical approach to the testing of the fission hypothesis, Astron. J. 82 (1977) 1013–1024.

[26] J. Stam, E. Fiume, Depicting fire and other gaseous phenomena using diffusion processes, Proceedings of the 22nd Annual Conference on Computer Graphics and Interactive Techniques (1995) 129–136.

[27] M. Müller, D. Charypar, M. Gross, Particle-Based Fluid Simulation for Interactive Applications, Proceedings of the 2003 ACM SIGGRAPH/Eurographics symposium on Computer animatio (2003) 154–159.

[28] J. J. Monaghan, Simulating free surface flows with SPH, J. Comput. Phys. 110 (1994) 399–406.

[29] H. Takeda, S. M. Miyama, M. Sekiya, Numerical simulation of viscous flow by smoothed particle hydrodynamics, Prog. Theor. Phys. 92 (5) (1994) 939–960.

[30] S. J. Watkins, A. S. Bhattal, N. Francis, J. A. Turner, A. P. Whitworth, A new prescription for viscosity in smoothed particle hydrodynamics, A & A S 119 (1996) 177–187.

[31] J. P. Morris, P. J. Fox, Y. Zhu, Modeling low Reynolds number incompressible flows using SPH, J. Comput. Phys. 136 (1997) 214–226.

[32] S. J. Cummins, M. Rudman, An SPH projection method, J. Comput. Phys. 152 (2) (1999) 584–607.

[33] S. Shao, E. Y. M. Lo, Incompressible SPH method for simulating Newtonian and non-Newtonian flows with a free surface, Adv. Water Res. 26 (2003) 787–800.

[34] P. W. Cleary, J. J. Monaghan, Conduction modelling using smoothed particle hydrodynamics, J. Comput. Phys. 148 (1999) 227–264.

[35] J. P. Morris, Simulating surface tension with smoothed particle hydrodynamics, Int. J. Numer. Meth. Fluids 33 (3) (2000) 333–353.

[36] J. J. Monaghan, SPH compressible turbulence, Mon. Not. R. Astron. Soc. 335 (2002) 843–852.

[37] D. Violeau, R. Issa, Numerical modelling of complex turbulent free-surface flows with the SPH method: an overview, Int. J. Numer. Meth. Fluids 53 (2) (2007) 277–304.

[38] R. A. Dalrymple, B. D. Rogers, Numerical modeling of water waves with the SPH method, Coastal Engng. 53 (2006) 141–147.

[39] M. Robinson, J. J. Monaghan, Direct numerical simulation of decaying two-dimensional turbulence in a no-slip square box using smoothed particle hydrodynamics, Int. J. Numer. Meth. Fluids 70 (1) (2012) 37–55.

[40] S. Børve, M. Omang, J. Trulsen, Regularized smoothed particle hydrodynamics: A new approach to simulating magnetohydrodynamic shocks, Astrophys. J. 561 (2001) 82–93.

41

[41] S. Børve, M. Omang, J. Trulsen, Regularized smoothed particle hydrody-
namics with improved multi-resolution handling, J. Comput. Phys. 208 (1)
(2005) 345–367.

[42] A. K. Chaniotis, D. Poulikakos, P. Koumoutsakos, Remeshed smoothed
particle hydrodynamics for the simulation of viscous and heat conducting
flows, J. Comput. Phys. 182 (1) (2002) 67–90.

[43] A. K. Chaniotis, D. Poulikakos, Y. Ventikos, Dual pulsating or steady slot
jet cooling of a constant heat flux surface, J. Heat Transfer 125 (2003)
575–586.

[44] A. Obeidat, S. P. A. Bordas, Three-dimensional remeshed smoothed parti-
cle hydrodynamics for the simulation of isotropic turbulence, Int. J. Numer.
Meth. Fluids 86 (2017) 1–9.

[45] G.-H. Cottet, E. Maitre, A level-set formulation of immersed boundary
methods for fluid-structure interaction problems, Math. Model Meth. Appl.
Sci. 16 (3) (2006) 415–438.

[46] A. Dupuis, P. Chatelain, P. Koumoutsakos, An immersed boundary-lattice-
Boltzmann method for the simulation of the flow past an impulsively
started cylinder, J. Comput. Phys. 227 (9) (2008) 4486–4498.

[47] G. Morgenthal, J. H. Walther, An Immersed Interface Method for the
Vortex-In-Cell Algorithm, Computers & Structures 85 (2007) 712–726.

[48] S. E. Hieber, P. Koumoutsakos, An immersed boundary method for
smoothed particle hydrodyamics of self-propelled swimmers, J. Comput.
Phys. 227 (2008) 8636–8654.

[49] S. E. Hieber, P. Koumoutsakos, A Lagrangian particle level set method,
J. Comput. Phys. 210 (2005) 342–367.

[50] Q. Liu, O. V. Vasilyev, A Brinkman penalization method for compressible flows in complex geometries, J. Comput. Phys. 227 (2007) 946–966.

[51] D. A. Nield, A. Bejan, Convection in Porous Media.

[52] O. M. Phillips, Flow and Reactions in Permeable Rocks, Cambridge University Press (1991) –.

[53] K. M., Principles of Heat Transfer in Porous Media, Springer-Verlag (1991) –.

[54] H. C. Brinkman, A calculation of the viscous force exerted by a flowing fluid on a dense swarm of particles, Appl. Sci. Res. 1 (1) (1949) 27–34.

[55] R. A. Wooding, Steady state free thermal convection of liquid in a saturated permeable medium, J. Fluid Mech. 2 (1957) 273–285.

[56] K. Vafai, C. L. Tien, Boundary and inertia effects on flow and heat transfer in porous media, Int. J. Heat Mass Transfer 24 (1981) 195–203.

[57] J. L. Beck, Convection in a box of porous material saturated with fluid, Phys. Fluids 15 (1972) 1377–1383.

[58] J. Smagorinsky, General circulation experiments with the primitive equations, part I: the bacis experiment, Monthly Weather Rev. 91 (3) (1963) 99–164.

[59] R. R. S., M. P., Numerical simulation of turbulent flows, Annu. Rev. Fluid Mech. 16 (1984) 99–137.

[60] M. J. J., Particle methods for hydrodynamics, Comput. Phys. Rep. 3 (1985) 71–123.

485 [61] U. Ghia, K. N. Ghia, C. T. Shin, High-Re solution for incompressible flow using the Navier-Stokes equations and a multigrid method, J. Comput. Phys. 48 (1982) 387–411.

[62] A. Obeidat, T. Schnipper, K. M. Ingvorsen, S. Haider, K. E. Meyer, M. Stefan, J. H. Walther, Large eddy simulations of the influence of piston position 490 on the swirling flow in a model two-stroke diesel engine, Int. J. Num. Meth. for Heat & Fluid Flow 24 (2) (2014) 325–341.

[63] S. Haider, T. Schnipper, A. Obeidat, K. E. Meyer, V. L. Okulov, S. Mayer, J. H. Walther, PIV study of the effect of piston position on the incylinder swirling flow during the scavenging process in large two-stroke 495 marine Diesel engines, J. Mar. Sci. Tech. 18 (2013) 133–143. `doi:10.1007/s00773-012-0192-z`.